MULTISPECTRAL IMAGING OF TISSUE ABLATION

Henryk Blasinski[†] *Jeff Caves*[⋆] *Joyce Farrell*[†] *Brian Wandell*[†] *Paul Wang*[⋆†]

[†] Department of Electrical Engineering, Stanford University
[⋆] Department of Bioengineering, Stanford University
[⋆†] Cardiovascular Medicine, Stanford School of Medicine

ABSTRACT

We describe a computational spectral imaging system that can acquire data in both the visible and near-infrared bands. We first show that the system is capable of estimating the full spectral reflectance of porcine tissue. We then show that the output of the system can be combined with machine learning algorithms to classify heart tissue that has been ablated for different amounts of time. The results of our analysis can be used to guide the design of an imaging system that can help cardiac electrophysiologists identify the position and efficacy of ablations during surgery.

Index Terms— Multispectral imaging, catheter ablation, atrial fibrillation, cardiac arrhythmia, ablation visualization

1. INTRODUCTION

Multispectral imaging is a quantitative approach to measuring tissue reflectance properties [1]. Instruments for measuring tissue in multiple wavelength bands can make discriminations about tissue type - including disease, blood oxygen, and the presence of molecular markers - that cannot be easily made by conventional RGB cameras or the human eye. In this paper, we describe a multispectral imaging system that can acquire data in both the visible and near-infrared bands and show how the system can be used to detect changes in porcine heart tissue after ablation. Our results suggest that multispectral imaging can provide diagnostic information during catheter ablation for atrial fibrillation.

Atrial fibrillation is a type of cardiac arrhythmia or heart rhythm problem that can cause stroke, shortness of breath or even heart failure [2]. The irregular heart contractions are caused by chaotic electrical activity in the atria.

One way to treat atrial fibrillation is to destroy the atrial cells surrounding the pulmonary veins (PV). This isolates the chaotic electrical activity and prevents it from spreading to other parts of the heart. During the procedure, the cardiologist positions a catheter and creates a series of ablative lesions surrounding the PV. Radiofrequency (RF) energy is commonly used to ablate the atrial tissue. Magnetic or impedance based systems are used to create a 3-dimensional map of the catheter electrode position in order to help the cardiologist apply a circumferential series of lesions surrounding the PVs. Variations in tissue contact and tissue thickness, as well as inaccuracies of the positioning system, make it difficult to complete a full circumferential lesion around the PVs. [3, 4]. This incompleteness is a major cause of the 20–30% rate of recurrence of atrial fibrillation [3].

Direct visual confirmation of a complete circumferential lesion would increase the success of the ablation procedure. A remaining challenge is that ablative tissue appears visually similar to non-ablated tissue. The damage from the ablation results in changes to the structure and chemical composition of the myocardial tissue [5, 6, 7, 8, 9, 10] and some of these changes are not visible to the human eye. Recent studies [11, 12, 13] suggest that ablated heart muscles exhibit different reflectance properties in the 700 to 900nm spectral band, well above the 700nm visibility threshold of the human eye.

We designed a multispectral imaging system with 14 spectral channels and sensitivity spanning from near UV to NIR. We combine the output of this system with machine learning algorithms to classify ablated tissue. The results of our analysis can be used to guide the design of an imaging system that can help cardiac electrophysiologists identify the position and efficacy of ablations during surgery, leading to more effective ablations and a reduced risk of complications.

2. METHODS

2.1. Multispectral imaging system

We built a prototype multispectral imaging system using a PointGrey Flea3 FL3-519U3-13Y3M-C monochrome, 1.3MP CMOS camera and a Schneider Optics Tele-Xenar 70mm lens. The camera is sensitive in the 400 to 1000nm wavelength range. The distance between the camera and the lens was increased by about 2cm to improve system magnification and to allow for high resolution imaging of small areas. The illumination was composed of 14 light emitting diodes (LEDs) with peak emissions spanning the near UV to near infrared (NIR) range [14]. The UV LEDs (365, 395nm) were manufactured by International Light Technologies. The visible LEDs (447, 470, 505, 530, 590, 627, 655nm) were

produced by Luxeon Star and the NIR LEDs (680, 780, 850, 880, 940nm) were from Epitex. Camera shutter and LEDs were synchronized by an external Arduino Mega 2560 controller. The camera frame rate of 150 frames per second combined with the LED power of about one watt made it possible to acquire a set of images under each light in about one second.

Pixel intensities $m \in \mathbf{R}^n$ captured by a monochrome camera at a particular spatial location, and under n illuminants are a linear function of the surface reflectance

$$m = L^T \mathbf{diag}(c) B w, \tag{1}$$

where $L \in \mathbf{R}^{q \times n}$ is a matrix whose columns represent spectral power distributions of the illuminants, $c \in \mathbf{R}^q$ is the spectral sensitivity of the sensor and Bw is a linear basis representation of the surface spectral reflectance [15]. In this representation the q dimensional reflectance vector is approximated with n_w number of fixed and known basis functions provided in $B \in \mathbf{R}^{q \times n_w}$. Reflectance estimation typically consists in solving a minimization problem [16]

$$\text{minimize} \;\; \|m - L^T \mathbf{diag}(c) B w\|_2^2 + \delta \|\nabla B w\|_2^2, \tag{2}$$

where $\|\nabla B w\|_2^2$ imposes a roughness penalty, controlled by adjustable parameter α, on the estimated reflectance. The matrix $\nabla \in \mathbf{R}^{q-1 \times q}$ computes differences between neighboring entries of a vector. The above minimization is a least-squares problem, where a solution

$$w = D^{\dagger} m, \qquad D = \left[B^T \mathbf{diag}(c) L \; B^T \nabla^T \right]^T, \tag{3}$$

is linear in the measured pixel intensities. The $\dagger$ denotes a Moore-Penrose inverse of a matrix.

2.2. Sample preparation

Pig ventricles were obtained from a butcher immediately prior to experimentation, sectioned into strips, and maintained in phosphate buffered saline (PBS) during processing. An ablation imaging template, consisting of strips of vinyl film punched with five circular holes (4mm interior diameter), was fixed in place over each strip of tissue. Tissue was briefly removed from PBS and ablated by placing an ablation electrode through the template holes to contact with the endocardial surface. Ablations were created with 40W of radiofrequency current for 15, 30, 45, or 60s. A single template region was left without ablation.

The images captured in each of the 14 spectral channels were spatially corrected for illuminant intensity nonuniformities. Reference light intensities were measured by capturing an image of a white Spectralon target. These corrected images were manually segmented, the same class label was assigned to all pixels within a particular stencil region of interest. We assume that tissue was spatially uniformly ablated with that area. During segmentation, shaded areas and specular reflections were avoided. Once segmented, each pixel was analyzed independently, its spatial location and surrounding pixel values were ignored. Overall, each ablation level was represented by about 35000 pixels.

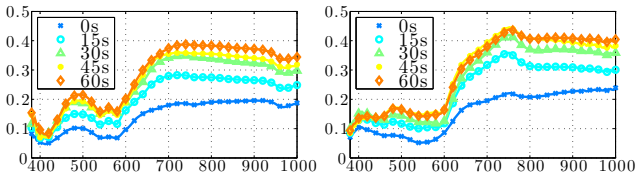

Fig. 1: Tissue reflectance comparison. Panels show tissue spectral reflectance estimated using a spectrophotometer (left) and the LED based, computational imaging system (right). In each plot the x-axis represents wavelength in nanometers, and color coding shows different ablation levels.

3. RESULTS

3.1. Reflectance estimation

Figure 1 compares reflectance spectra estimated by analysis of image data captured by our multispectral imaging system with reflectance spectra measured by a SpectraScan PR715 spectrophotometer using a 0.5° degree aperture. Each curve represents a reflectance spectrum for a particular ablation duration averaged over all the tissue samples and pixels belonging to each ablation category. Spectral reflectances were calculated by dividing the spectral radiance reflected from the tissue by the spectral power of the illumination. The tissue reflectances estimated by the multispectral imaging system are similar in shape to tissue reflectances measured by the PR715 spectrophotometer and both approaches show that the amount of reflected light increases with ablation time.

3.2. Pixel classification

Differences in reflectance spectra can be used in classification algorithms to determine the ablation level from tissue appearance. Reflectance spectra are linearly related to measured pixel intensities, therefore, with little influence on algorithm performance, pixel values can be used instead as inputs. The results we describe in this section are based on direct analysis of the 14 channel data, which can be treated as a low dimensional representation of reflectance spectra [17].

To evaluate classification performance, we selected seven standard machine learning algorithms: Support Vector Machine (SVM), Naive Bayes (NB), Linear Discriminant Analysis (LDA), Multinomial Logistic Regression (LR), Quadratic Discriminant Analysis (QDA), Classification Tree (Tree) and k-Nearest Neighbors (KNN). All algorithms were implemented in Matlab using the Machine Learning toolbox (the only exception is the SVM for which we used the libsvm package [18]). The classifiers are listed in increasing order

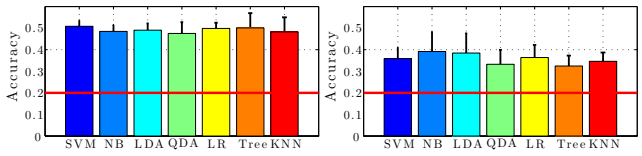

Fig. 2: 5-way tissue classification accuracy for multispectral (left), RGB (right) and random guess (both pannels, red line).

of flexibility, where the simplest ones (SVM, NB, LDA, LR) select hyperplanes separating different classes, and the most flexible ones can derive decision surfaces of arbitrary shapes (KNN).

Classification tasks were analyzed using leave-one-out (LOO) cross validation. The data is first split into four subsets corresponding to each of the samples. Next, three subsets are combined, and classifiers are tuned via stratified 10-fold cross validation uniquely on that combined subset. The stratified 10-fold cross validation method splits the data into 10 non-overlapping subsets. Within each subset, also called a fold, the class probability distribution is preserved. The results are averaged over 10 trials, so that each individual fold is used as test data, and the remaining nine folds serve for classifier training. Finally, the accuracy is reported for the fourth subset unseen during training and validation [19].

As a basis for comparisons we estimated the data that would be obtained using a conventional RGB camera. To do this, we used tissue reflectance spectra, estimated with the multispectral imaging system, as input to a computer simulation of a Nikon D1 digital camera [20].

Figure 2 presents the 5-way classification results for multispectral and RGB data. The advantage of using spectral data is clear as it offers performance gains of about 10 percentage points. All algorithms achieve about 50% accuracy and perform substantially better than random guessing at 20%. The nonlinear classification methods; KNN and Tree, do not exhibit higher classification performance than the simpler linear classifiers. The spatial arrangement of classification outcomes is presented in Fig. 3, where colors correspond to different classes. The 45s and 60s ablation classes appear to be the most confusing.

3.3. System design

Active illumination systems do not capture individual channel images at the same time instance. Consequently imaged objects can shift their positions between consecutive frame acquisitions causing errors in reflectance estimates. A faster camera or a system with fewer channels can reduce these alignment errors and be less costly to manufacture. For these reasons it is advantageous to limit the number of spectral channels used for imaging, assuming that this reduction does not impact the overall system performance.

To test the influence of the number of channels on classification accuracy, we conducted a backward stepwise selection procedure. At every step of this iterative procedure the LED channel that is the least correlated with the predicted label is removed from the classifier input data [17]. Figure 4 plots classification performance as a function of the number of channels used. Note that all the curves plateau when data from the best three to four channels are available to the classifiers. Furthermore, classification algorithms that use the three best channels achieve accuracy of about 50% which outperforms conventional RGB camera (Fig. 2). Spectral channel selection is consistent across different algorithms. The most informative channels are those captured in the 850-880nm, 655-680nm and 505-530nm bands. Two algorithms, KNN and QDA, also include the UV channel 365nm among their top three selections.

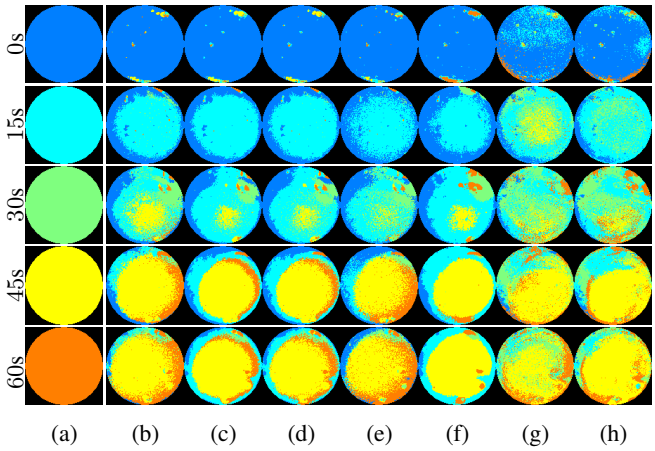

Fig. 3: Example tissue patch classification for different ablation times (rows), 0s (top) through 60s (bottom) and classification outcomes (columns) ground truth (a), SVM, NB, LDA, QDA, MLR, Tree and KNN (b–h).

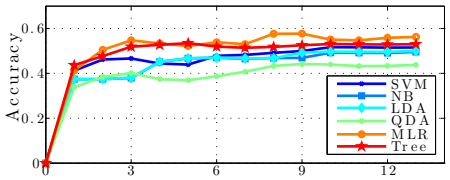

Fig. 4: Tissue classification for custom systems with different number of spectral channels (x-axis). A well designed three channel system outperforms conventional RGB cameras.

4. DISCUSSION

We compared the tissue reflectance estimated by a spectrophotometer with the estimates obtained using an LED based multispectral imaging system. The spectra obtained using the two approaches are similar and show that the increase in the amount of reflected light with ablation time is

present over the entire spectral range. These similarities indicate that the data captured with the LED based system can be used as input for machine learning classifiers.

Our analysis of the multispectral image data show that classification gains can be achieved using custom, three channel systems rather than commercial RGB cameras. Our simulations showed that custom systems capturing light with wavelengths around 850 and 680nm, *i.e.* the spectral bands that were consistently selected in a backward stepwise selection procedure, performed better than a commercial RGB camera.

Our study also identified three interesting areas for future research. First, we observed that the spectral reflectance functions for 45s and 60s ablation durations are similar. This is further supported by classification results; the two cases are often confused for one another. This result may suggest that an ablation time of 45s is long enough to damage the tissue and that longer ablation times are not necessary. Second, spatial arrangements of incorrectly classified pixels imply that the tissue may not have been uniformly ablated within the area of interest and motivates spatially dependent investigations. Finally, the backward stepwise selection procedure applied to two classifiers selected the channel with the LED peak emission wavelength of 365nm among the top three informative channels, though our imaging system could not detect light with such short wavelengths. This result may imply that the UV light excites fluorescence in the sample, which is then emitted in the longer wavelengths detectable by our sensor.

5. REFERENCES

[1] K. Zuzak, R. Francis, E. Wehner, M. Litorja, J. Cadeddu, and E. Livingston, "Active DLP hyperspectral illumination: a noninvasive, in vivo, system characterization visualizing tissue oxygenation at near video rates," *Analytical chemistry*, vol. 83, no. 19, pp. 7424–7430, 2011.

[2] D. Lloyd-Jones, R. Adams, T. Brown, M. Carnethon, S. Dai, G. De Simone, B. Ferguson, E. Ford, K. Furie, C. Gillespie, et al., "Heart disease and stroke statistics - 2010 update a report from the american heart association," *Circulation*, vol. 121, no. 7, pp. e46–e215, 2010.

[3] A. Auricchio, J. Singh, and F. Rademakers, *Cardiac Imaging in Electrophysiology*, Springer Science & Business Media, 2011.

[4] A. Schade, J. Krug, A. Szöllösi, M. El Tarahony, and T. Deneke, "Pulmonary vein isolation with a novel endoscopic ablation system using laser energy," 2012.

[5] S. Thomsen, S. Jacques, and S. Flock, "Microscopic correlates of macroscopic optical property changes during thermal coagulation of myocardium," in *OE/LASE'90, 14-19 Jan., Los Angeles, CA*. International Society for Optics and Photonics, 1990, pp. 2–11.

[6] R. Splinter, R. Svenson, L. Littmann, J. Tuntelder, C. Chuang, G. Tatsis, and M. Thompson, "Optical properties of normal, diseased, and laser photocoagulated myocardium at the nd:yag wavelength," *Lasers in Surgery and Medicine*, vol. 11, no. 2, pp. 117–124, 1991.

[7] J. Pickering, S. Bosman, P. Posthumus, P. Blokland, J. Beek, and M. van Gemert, "Changes in the optical properties (at 632.8nm) of slowly heated myocardium," *Appl. Optics*, vol. 32, no. 4, pp. 367–371, 1993.

[8] A. Nilsson, C. Sturesson, D. Liu, and S. Andersson-Engels, "Changes in spectral shape of tissue optical properties in conjunction with laser-induced thermotherapy," *Appl. Optics*, vol. 37, no. 7, pp. 1256–1267, 1998.

[9] R. Agah, A. Gandjbakhche, M. Motamedi, R. Nossal, and R. Bonner, "Dynamics of temperature dependent optical properties of tissue: dependence on thermally induced alteration," *IEEE Trans. on Biomedical Engineering*, vol. 43, no. 8, pp. 839–846, 1996.

[10] J. Swartling, S. Paalsson, P. Platonov, S. Olsson, and S. Andersson-Engels, "Changes in tissue optical properties due to radio-frequency ablation of myocardium," *Medical and Biological Engineering and Computing*, vol. 41, no. 4, pp. 403–409, 2003.

[11] S. Demos and S. Sharareh, "Real time assessment of RF cardiac tissue ablation with optical spectroscopy," *Optics express*, vol. 16, no. 19, pp. 15286–15296, 2008.

[12] H. Yoshimura, J. Viator, and S. Jacques, "Relationship between damaged fraction and reflected spectra of denaturing tissues," *Lasers in surgery and medicine*, vol. 37, no. 4, pp. 308–313, 2005.

[13] R. Singh-Moon and C. Hendon, "Towards optical monitoring of radiofrequency ablation extent for atrial fibrillation," in *IEEE 12th International Symposium on Biomedical Imaging, ISBI*. IEEE, 2015, pp. 751–755.

[14] M. Parmar, S. Lansel, and J. Farrell, "An LED-based lighting system for acquiring multispectral scenes," in *Proc. SPIE*, 2012, vol. 8299, pp. 82990P–82990P–8.

[15] L. Maloney and B. Wandell, "Color constancy: a method for recovering surface spectral reflectance," *Journal of the Optical Society of America A*, vol. 3, no. 1, pp. 29–33, 1986.

[16] H. Blasinski, J. Farrell, and B. Wandell, "An iterative algorithm for spectral estimation with spatial smoothing," in *IEEE International Conference on Image Processing, ICIP*, Sept 2015, pp. 936–940.

[17] T. Hastie, R. Tibshirani, and J. Friedman, *The elements of statistical learning*, Springer, 2009.

[18] C. Chang and C. Lin, "LIBSVM: A library for support vector machines," *ACM Transactions on Intelligent Systems and Technology*, vol. 2, pp. 27:1–27:27, 2011.

[19] G. Forman and M. Scholz, "Apples-to-apples in cross-validation studies: pitfalls in classifier performance measurement," *ACM SIGKDD Explorations Newsletter*, vol. 12, no. 1, pp. 49–57, 2010.

[20] J. Farrell, F. Xiao, P. Catrysse, and B. Wandell, "A simulation tool for evaluating digital camera image quality," in *Electronic Imaging 2004*, 2003, pp. 124–131.